Published in Laser Physics, 2010, Vol. 20, No. 3, pp. 581-590

# Numerical calculation of strong-field laser-atom interaction: An approach with perfect reflection-free radiation boundary conditions.

M. Heinen*
*Institute of Solid State Research, Soft Condensed Matter, Research Centre Jülich, 52425 Jülich, Germany*

H.-J. Kull†
*Institute of Theoretical Physics A, RWTH Aachen University, Templergraben 55, 52056 Aachen, Germany*

(Dated: February 25, 2010)

The time-dependent, single-particle Schrödinger equation with a finite-range potential is solved numerically on a three-dimensional spherical domain. In order to correctly account for outgoing waves, perfect reflection-free radiation boundary conditions are used on the surface of a sphere. These are computationally most effective if the particle wavefunction is expanded in the set of spherical harmonics and computations are performed in the Kramers-Henneberger accelerated frame. The method allows one to solve the full ionization dynamics in intense laser fields within a small region of atomic dimensions.

PACS numbers: 31.15.xf, 32.80.Rm

## I. INTRODUCTION

Finite-difference methods have become an important tool for the study of strong-field laser-atom interactions. Investigations of above threshold ionization (ATI) and high-order harmonic generation (HOHG) in general require the solution of the time-dependent Schrödinger equation (TDSE) for a single-electron atom coupled to a strong radiation field mostly in the dipole approximation. In this context, the finite-difference method was first introduced in early work on multi-photon ionization of hydrogen [1]. In the past, various approaches based on implicit finite-difference schemes [2, 3], B-spline representations [4, 5], angular momentum decompositions [6–9], Fourier-methods [10, 11] and different gauges [12] have been proposed.

One of the limitations of the finite-difference approach arises from the necessarily finite spatial domain that can be represented on computational grids. The propagation distance of electrons accelerated by ultrashort laser pulses can largely exceed the characteristic range of the atomic potential. Therefore, in most cases, the wavefunction has to be artificially damped towards the boundaries in order to minimize residual reflections into the computational region. Although there exist a number of quite reasonable boundary techniques, based e.g. on imaginary potentials [13, 14], complex coordinates [15] or mask-functions [16], it should be noted that they are not perfect and mostly have to be adapted to each particular case.

In the present work, it is our purpose to replace absorbing boundary regions entirely by perfect reflection-free boundary conditions for the TDSE. One of the difficulties with these boundary conditions arises from the dispersion of waves as described by the dispersion relation $k = k(\omega)$. It is only in the absence of dispersion, $k(\omega) = \omega$, that one can obtain a simple linear relationship $\partial_z = -\partial_t$ between the derivatives of outgoing waves in the position and time domain. Unfortunately, the dispersion relation $k = \sqrt{2\omega}$ for the TDSE cannot be replaced in the same manner by a local derivative expression.

In general, the outgoing wave boundary conditions are nonlocal in space and time [17]. Nonlocal boundary conditions have already been successfully used in a number of 1D calculations [18–21], however, the generalization to three dimensions and the inclusion of the laser interaction, lacking spherical symmetry, requires substantial modifications. In a first step, the present boundary conditions have been generalized from 1D to 3D without laser field [22]. We refer to this work for details to the boundary conditions and for further references. This method has been applied to spherically symmetric quantum tunneling for different uncoupled angular momentum quantum states. In the next step, reported in this work, the laser field has been included and the feasibility of the method for strong-field photoionization of atoms with coupled angular momentum states has been demonstrated.

The present boundary conditions are not to be mis-

*m.heinen@fz-juelich.de
†kull@ilt-extern.fraunhofer.de

understood as an all purpose method. Actually, a computational strategy has to be developed that best fits to the boundary constraints. We point out some of the restrictions posed by the method. In the present work the boundary conditions are derived in three dimensions on the surface of a sphere. Thereby it is assumed, that both the initial wave-function and the potential are zero in the region exterior to the sphere. In other words, the wavefunction reaches the exterior region only by transmission through the boundary and the transmitted part then propagates freely without further interaction. For this relatively simple geometry, the propagator for the exterior region can be analytically calculated without approximations. Due to the spherical symmetry of the boundary we use spherical coordinates and an expansion of the wavefunction in spherical harmonics. Long range potentials with populations in highly excited Rydberg states cannot be adequately treated by the method. To avoid such difficulties, we restrict attention to potentials of finite range or with an exponential screening length. In addition, the interaction with the laser field has to be avoided in the exterior region. This restriction leads us to consider the laser interaction in the Kramers-Henneberger (KH) accelerated reference frame [23, 24]. In this frame, the asymptotic quiver motion of the electron is absent, being transferred to the atomic potential. In contrast to most other numerical TDSE calculations the present computations are therefore not performed in the velocity or length gauge but in the KH frame. The numerical algorithm in the KH frame is similar to the one in [25].

Atomic units will be used throughout this paper, such that $h/2\pi = m = -q = 1$ ($h$: Planck-constant, $m$: particle mass, $q$: particle charge).

## II. RADIATION BOUNDARY CONDITIONS

The wave function $\psi(\mathbf{r},t)$ of a classical particle interacting with a time-dependent potential $V(\mathbf{r},t)$ is governed by the TDSE

$$i\partial_t\psi(\mathbf{r},t) = \left[-\frac{1}{2}\Delta + V(\mathbf{r},t)\right]\psi(\mathbf{r},t). \tag{1}$$

In the following, we are going to introduce a method to calculate the time evolution of a given initial wave function $\psi(\mathbf{r},0)$ within a sphere $r \le R$. Spherical coordinates $\mathbf{r} = (r,\theta,\phi)$ will be used and the wave function and potential will have to satisfy

$$\left.\begin{array}{l}\psi(\mathbf{r},0) = 0\\ V(\mathbf{r},t) = 0\end{array}\right\} \quad \text{for} \quad r \ge R. \tag{2}$$

We are especially interested in unbounded solutions reaching the boundary $r = R$ during the time interval under consideration. To avoid unphysical reflections of the wave-function from this boundary, we will employ perfect reflection-free boundary conditions that have been derived in detail in [22]. We therefore restrict ourselves here to a brief summary of the keypoints in this derivation.

Instead of solving directly for the wave-function $\psi$ in real space, we choose the function $\phi(\mathbf{r},t) = r\psi(\mathbf{r},t)$ and expand it in the basis of spherical harmonics $Y_l^m$,

$$\phi(r,\theta,\varphi,t) \;=\; \sum_{l=0}^{\infty}\sum_{m=-l}^{l} \phi_l^m(r,t)Y_l^m(\theta,\varphi). \tag{3}$$

We now consider the solution in the region $r > R$ exterior to the sphere. The radial part of each harmonics satisfies the well-known $1D$-TDSE with an effective centrifugal-barrier potential,

$$\begin{aligned} M_l(r,t)\phi_l^m(r,t) \;&=\; 0 \\ M_l(r,t) \;&=\; i\partial_t + \frac{1}{2}\partial_r^2 - \frac{l(l+1)}{2r^2}. \end{aligned} \tag{4}$$

The appropriate solution is subject to the initial and boundary values

$$\phi_l^m(r,0) = 0 \qquad \text{for} \qquad r > R, \qquad \phi_l^m(\infty,t) = 0. \tag{5}$$

The present 3D-problem differs from the 1D-problem, treated previously in [18], by the presence of the effective potential $l(l+1)/(2r^2)$. We will recover the 1D result in the special case $l = 0$ and in the limiting case $R \to \infty$ later in this section.

Following the Green's function formalism [18, 22], the solution of (4) at any coordinate $r \ge R$ and time $t \ge 0$ can be calculated as

$$\phi_l^m(r,t) = \frac{1}{2}\int_0^t d\tau H_l(r,R,\tau)\partial_{r'}\phi_l^m(r',t-\tau)\big|_{r'=R}, \tag{6}$$

with $H_l(r,r',\tau)$ being the Green's function of the operator $M_l$, defined by [22]

$$M_l(r',\tau)H_l(r,r',\tau) = \delta(r-r')\delta(\tau), \tag{7a}$$

$$H_l(r,r',\tau) = 0, \qquad \text{for} \quad \tau \le 0, \tag{7b}$$

$$\partial_{r'}H_l(r,r',\tau)\big|_{r'=R} = 0, \tag{7c}$$

$$\int_0^\infty dt' \;\left\{H_l\partial_{r'}\phi_l' - \phi_l'\partial_{r'}H_l\right\}\big|_{r'\to\infty} = 0, \tag{7d}$$

and with $\delta(x)$ denoting the Dirac delta function. Equation (6) implies that the Dirichlet boundary value $\eta_l^m(t) = \phi_l^m(R,t)$ of the solution can be calculated from the time history of the Neumann boundary value $\gamma_l^m(t) = \partial_r\phi_l^m(r,t)\big|_{r=R}$ as

$$\eta_l^m(t) = \frac{1}{2}\int_0^t d\tau H_l(R,R,\tau)\gamma_l^m(t-\tau). \tag{8}$$

The partial differential equation (7a) can be solved by the method of Laplace transformation. We define the

Laplace-transform $\hat{f}(\omega)$ of a function $f(t)$ that fulfills $f(t) = 0$ for $t < 0$ and $|f(t)| < e^{ct}$ for $t \to \infty$ as

$$\hat{f}(\omega) = \int_0^\infty dt f(t) e^{i\omega t}, \qquad \Im\{\omega\} \geq c.$$

The so-transformed equation (7a) is an ordinary differential equation, the solutions of which have been identified in [22] as

$$\hat{H}_l(R, R, \omega) = \frac{2}{k} \frac{\rho h_l^{(1)}(\rho)}{\partial_\rho \left[\rho h_l^{(1)}(\rho)\right]}\Bigg|_{\rho=kR}. \tag{9}$$

Here, $k = \sqrt{2\omega}$, $\rho = kr$, and $h_l^{(1)}$ are the spherical Hankel functions [26]. For a simple back-transformation of the solution (9) from the complex frequency-domain into the time-domain, we use a polynomial representation of the Hankel functions and a recurrence relation of their derivatives [22, 26] to write (9) as a rational function in complex frequency-space,

$$\begin{aligned}\hat{H}_l \;=\; & \frac{2}{k} \sum_{\nu=0}^{l} \left(l + \frac{1}{2}, \nu\right) (-2ikR)^{-\nu} \\ & \times \left[\sum_{\nu=0}^{l} (l+1) \left(l + \frac{1}{2}, \nu\right) (-2i)^{-\nu} (kR)^{-\nu-1} \right. \\ & \left. + i \sum_{\nu=0}^{l+1} \left(l + \frac{3}{2}, \nu\right) (-2ikR)^{-\nu}\right]^{-1}, \end{aligned} \tag{10}$$

with coefficients

$$\left(l + \frac{1}{2}, \nu\right) = \frac{(l+\nu)!}{\nu! \Gamma(l - \nu + 1)}.$$

Expression (10) can be numerically expanded in partial fractions. It shows $l + 1$ simple poles $k = \kappa_j^{(l)}$, so that the result can be written as

$$\hat{H}_l(R, R, \omega) = 2 \sum_{j=1}^{l+1} \frac{\gamma_j^{(l)}}{k - \kappa_j^{(l)}}. \tag{11}$$

The inverse Laplace transform of (11) can be found in tables [26]. It is given by

$$H_l(R, R, \tau) = 2 \sum_{j=1}^{l+1} \gamma_j^{(l)} \left\{ \frac{1}{\sqrt{2\pi i \tau}} - i \frac{\kappa_j^{(l)}}{2} w(z_j^{(l)}) \right\},$$

where $z_j^{(l)} = -\kappa_j^{(l)} \sqrt{i\tau/2}$ and $w(z) = \exp(-z^2)\mathrm{erfc}(-iz)$. By comparison of (11) and the Hankel functions in (9) for high values of $k$, it can be shown [22] that

$$\sum_{j=1}^{l+1} \gamma_j^{(l)} = -i.$$

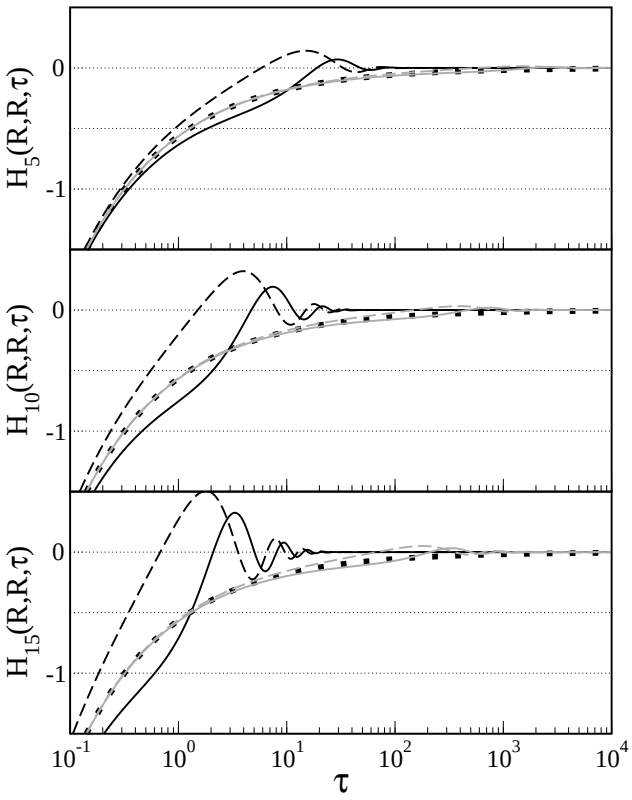


FIG. 1: Real (solid line) and imaginary part (dashed) of the Green's function (12) for various quantum numbers $l$. Black curves correspond to $R = 10$, grey curves to $R = 100$. The solution for $l = 0$, which does not dependent on $R$ and is identical to the Green's function of a 1D half-space is shown as the dotted curve.

This allows one to further simplify the Green's function to our final result

$$H_l(R, R, \tau) = \frac{-2i}{\sqrt{2\pi i \tau}} - i \sum_{j=1}^{l+1} \gamma_j^{(l)} \kappa_j^{(l)} w(z_j^{(l)}). \tag{12}$$

The first, l-independent part of (12) is the Green's function of a 1D half-space, which was already derived in [18]. This 1D result is contained in (12) in the special case $l = 0$, since $\kappa_1^{(0)} = 0$. The 1D result is also recovered in the limiting case $R \to \infty$ for all finite quantum numbers $l$, because the centrifugal barrier $l(l+1)/(2r^2)$ vanishes at infinite radii. Plots of $H_l(R, R, \tau)$ for $l = 0, 5, 10, 15$ and $R = 10, 100$ are shown in Fig. 1. For higher angular momentum quantum numbers one can observe stronger oscillations and faster decay.

## III. NUMERICAL SOLUTION METHOD

In this section we are going to describe a numerical algorithm for the solution of (1) in the domain $r \leq R$,

based on the boundary condition (8) with the Green's function (12). As in the previous section, we choose to solve for the expansion coefficients $\phi_l^m(r,t)$ of the wavefunction, given in (3). The potential $V(\mathbf{r},t)$ is likewise expanded

$$V(\mathbf{r},t) = \sum_{l=0}^{\infty}\sum_{m=-l}^{l} V_l^m(r,t)Y_l^m(\theta,\varphi) \tag{13}$$

$$V_l^m(r,t) = \int d\Omega V(\mathbf{r},t){Y^*}_l^m(\Omega). \tag{14}$$

Here, the star denotes the complex conjugate and $\Omega$ is the solid angle with the volume element $d\Omega = \sin\theta d\theta d\varphi$.

Using the orthonormality relation of spherical harmonics, the TDSE can be written as an infinite set of coupled equations in the space of quantum numbers $l$ and $m$,

$$i\partial_t\phi_{l_1}^{m_1}(r,t) = \left[-\frac{1}{2}\partial_r^2 + \frac{l_1(l_1+1)}{2r^2}\right]\phi_{l_1}^{m_1}(r,t) + \sum_{\substack{l_2,m_2\\ l_3,m_3}} V_{l_3}^{m_3}(r,t)\phi_{l_2}^{m_2}(r,t)\int d\Omega {Y^*}_{l_1}^{m_1}(\Omega)Y_{l_2}^{m_2}(\Omega)Y_{l_3}^{m_3}(\Omega), \tag{15}$$

where the indexrange of the sum is $l_i = 0\ldots\infty, m_i = -l_i\ldots l_i$. We will use the same convention for all following sums if not otherwise stated. Furthermore the integral over solid angle of the product of three spherical harmonics is denoted by

$$W_{l_1,l_2,l_3}^{m_1,m_2,m_3} = \int d\Omega Y_{l_1}^{m_1}(\Omega)Y_{l_2}^{m_2}(\Omega)Y_{l_3}^{m_3}(\Omega) \tag{16}$$

These coefficients can be expressed by Wigner $3j$-symbols as [27]

$$W_{l_1,l_2,l_3}^{m_1,m_2,m_3} = \sqrt{\frac{(2l_1+1)(2l_2+1)(2l_3+1)}{4\pi}}\times \begin{pmatrix} l_1 & l_2 & l_3\\ 0 & 0 & 0\end{pmatrix}\begin{pmatrix} l_1 & l_2 & l_3\\ m_1 & m_2 & m_3\end{pmatrix}. \tag{17}$$

The Schrödinger equations can now be re-written as

$$i\partial_t\phi_l^m(r,t) = \sum_{l',m'}\mathcal{H}_{l',m'}^{l,m}(r,t)\phi_{l'}^{m'}(r,t), \tag{18}$$

$$\mathcal{H}_{l_2,m_2}^{l_1,m_1}(r,t) = \left[-\frac{1}{2}\partial_r^2 + \frac{l_1(l_1+1)}{2r^2}\right]\delta_{l_1l_2}\delta_{m_1m_2} + (-1)^{m_1}\sum_{l_3,m_3} W_{l_1,l_2,l_3}^{-m_1,m_2,m_3}V_{l_3}^{m_3}(r,t), \tag{19}$$

where $\delta_{ij}$ is the Kronecker Delta. For numerical solution, the expansion (3) must be truncated at a finite quantum number l, and the functions $\phi_l^m(r,t)$ must be discretized on a finite grid, which we choose to construct by equidistant steps in time and space

$$\begin{aligned} t_x &= x\Delta t, \qquad x = 0\ldots X,\\ r_y &= (y+1)\Delta r, \qquad y = 0\ldots Y,\\ &l = 0\ldots L. \end{aligned} \tag{20}$$

Note that the point $r = 0$ does not belong to the grid since $\phi_l^m(0,t) = r\psi_l^m(r,t)|_{r=0} = 0\ \forall t$, and that the expansion (13) may be truncated at $l = 2L$ without causing any further truncation error, because of the selection rules of the Wigner $3j$-symbols. The differential operator $\partial_r^2$ is discretized using the centre-point rule,

$$\partial_r^2 f(r_y) = (\Delta r)^{-2}\left[f(r_{y-1}) - 2f(r_y) + f(r_{y+1})\right] + \mathcal{O}(\Delta r^2),$$

so that the discretized version of $\mathcal{H}_{l',m'}^{l,m}(r,t)$ at a fixed point in time $t = t_x$ becomes a six-dimensional (6D) matrix $\mathbf{H}^x = \mathbf{H}^x_{l,l',m,m',y,y'}$, which is tridiagonal in each indexplane $(y,y')$. Correspondingly, the set of discretized functions $\phi_l^m(r,t)$ at time $t = t_x$ forms a three-dimensional matrix, which we denote by $\mathbf{\Phi}^x = \mathbf{\Phi}^x_{l,m,y} = \phi_l^m(r_y,t_x)$.

The discretization of the boundary condition (8), (12), begins with the Dirichlet and Neumann boundary values at the radial position $R = (Y+\frac{1}{2})\Delta r$,

$$\left.\begin{aligned} \eta_l^m(t_x) &= \frac{\phi_l^m(r_Y,t_x) + \phi_l^m(r_{Y-1},t_x)}{2}\\ \gamma_l^m(t_x) &= \frac{\phi_l^m(r_Y,t_x) - \phi_l^m(r_{Y-1},t_x)}{\Delta r}\end{aligned}\right\} + \mathcal{O}(\Delta r^2).$$

The Green's function (12) shows a square-root singularity for $\tau\to 0$, which may cause difficulties in the numerical integration of (8). We therefore use (5) in a partial integration to gain the representation

$$\eta_l^m(t_x) = \int_0^t d\tau\left(\sqrt{\frac{2i\tau}{\pi}}\partial_\tau + \mu_l(R,\tau)\right)\gamma_l^m(t_x-\tau), \tag{21}$$

$$\mu_l(R,\tau) = -\frac{i}{2}\sum_{j=0}^{l+1}\gamma_j^{(l)}\kappa_j^{(l)}w(z_j^{(l)}),$$

of the transparent boundary condition, which is well-suited for numerical integration. Discretization of (21) by the trapezoidal rule yields

$$\Xi_l^m(t_{x-1}) = \left[\mathbb{1} - \Lambda - \frac{2\Delta t}{\Delta r}\mu_l(R,0)\right]\phi_l^m(r_Y,t_x) + \left[\mathbb{1} + \Lambda + \frac{2\Delta t}{\Delta r}\mu_l(R,0)\right]\phi_l^m(r_{Y-1},t_x) + \mathcal{O}(\Delta r^2,\Delta t^2), \tag{22}$$

where

$$\Lambda = \frac{-2}{\Delta r}\sqrt{\frac{i\Delta t}{\pi}},$$

$$\begin{aligned}\Xi_l^m(t_{x-1}) \;=\; & \Lambda\left[\phi_l^m(r_{Y-1},t_{x-1})-\phi_l^m(r_Y,t_{x-1})\right]+\\ & \sum_{\nu=1}^{x-1}\Lambda\sqrt{2\nu+1}\left[\phi_l^m(r_{Y-1},t_{x-\nu-1})\right.\\ & \qquad\left.-\phi_l^m(r_Y,t_{x-\nu-1})\right]+\\ & \sum_{\nu=1}^{x-1}\left[\Lambda\sqrt{2\nu+1}+\frac{2\Delta t}{\Delta r}\mu_l(R,t_\nu)\right]\times\\ & \left[\phi_l^m(r_Y,t_{x-\nu})-\phi_l^m(r_{Y-1},t_{x-\nu})\right].\end{aligned}$$

Since the solution at the boundary is only coupled to its nearest neighbour, the $(y,y')$-indexplanes of the discretized Hamiltonians keep their tridiagonal form if (22) is applied. The computation of each $\Xi_l^m(t_{x-1})$ requires a summation of $\mathcal{O}(x)$ numbers at each timestep $x$ of a numerical algoritm, such that the total number of arithmetic operations required for the solution of (18),(22) on the grid (20) will contain a contribution of the order $(L+1)^2(X+X^2)$, caused by the evaluation of the boundary condition.

As the discretized Hamiltonian with transparent boundary conditions is now specified, the only remaining task for a complete discretization of (18) on the grid (20) is to choose one of the many existing finite difference time-stepping schemes [28]. Here we adopt the Crank-Nicolson (CN) [3] approach, which is commonly used for time integration of the TDSE, because it is known to be numerically stable and to provide unitary time evolution under hermitian Hamiltonians. The CN-scheme reads

$$\left(\mathbb{1}+\frac{i\Delta t}{2}\mathbf{H}^{x+1/2}\right)\mathbf{\Phi}^{x+1}=\left(\mathbb{1}-\frac{i\Delta t}{2}\mathbf{H}^{x+1/2}\right)\mathbf{\Phi}^{x}, \tag{23}$$

and shows the same discretization error as the boundary condition (22). The discretization error of the overall algorithm therefore stays of the order $\mathcal{O}(\Delta r^2,\Delta t^2)$.

The 6D-matrix $(\mathbb{1}+i\Delta t/2\mathbf{H}^{x+1/2})$ is densely populated in all indexplanes $(l,l')$ and $(m,m')$ if we assume the most general case of (14). To solve (23) efficiently on a computer, it is therefore most advisable to circumvent the contained inversion of this full matrix. One might choose a 3D Alternating Direction Implicit (ADI) method [28], that reduces the computational task to a series of inversions of and multiplications with 2D matrices in each of the three dimensions $l,m,y$, while conserving the discretization error of the CN-scheme. A neccessary condition for the use of the ADI method is the separability of the underlying CN-scheme. This condition is satisfied by (23) since the Hamiltonian splits into the sum of operators (19) and the boundary condition (8) is local in each of the quantum numbers $l$ and $m$.

However, the boundary condition (8) is independent of the quantum number $m$, and therefore we will restrict ourselves in the following sections to the solution of problems with azimuthal symmetry, in which all functions $V_l^m(r,t)$ with $m\neq 0$ vanish. In such problems, there will be no coupling of partial waves $\phi_l^m,\phi_{l'}^{m'}$ if $m\neq m'$, and the CN scheme can be solved by a 2D ADI method in the dimensions $l,y$.

## IV. PHOTOIONIZATION IN THE KRAMERS-HENNEBERGER FRAME

In this section we are going to apply the numerical solution algorithm of Sec. III to laser-induced excitation of particles initially bound to a finite-range central potential. The laser field will enter the calculations in electric dipole approximation. This system is viewed as a model for the photoionization of single atoms.

The TDSE for the wavefunction $\psi_{len}$ of a particle interacting with a potential $V(r)$ and an electric dipole field $\mathbf{E}(t)$ in the so-called length gauge reads

$$i\partial_t\psi_{len}(\mathbf{r},t)=\left[-\frac{1}{2}\Delta+V(r)+\mathbf{E}(t)\cdot\mathbf{r}\right]\psi_{len}(\mathbf{r},t). \tag{24}$$

While it allows the most straightforward interpretation of the resulting wavefunction in the laboratory frame with a fixed position of the potential, and an operator $\mathbf{p}=-i\nabla$ returning directly the mechanical momentum of the particle, the length gauge is often inappropriate for numerical computations [6, 12, 29]. One very obvious source of problems in the numerical solution of (24) is the term $\mathbf{E}(t)\cdot\mathbf{r}$, that increases to arbitrarily high values at large distances, thereby causing rapid phase-oscillations of the wavefunction that would have to be resolved in very small timesteps. Furthermore, the solution of (24) converges only very slowly as a function of L, if the wavefunction is expanded like (3) on a grid (20) [12]. For these reasons, present solution methods for the TDSE with intense laser fields [6, 7] are often formulated in the velocity gauge

$$i\partial_t\psi_{vel}(\mathbf{r},t)=\left[-\frac{1}{2}\Delta+V(r)-\frac{i}{c}\mathbf{A}(t)\cdot\nabla\right]\psi_{vel}(\mathbf{r},t), \tag{25}$$

where $c$ is the speed of light and $\mathbf{A}$ is the electromagnetic vector potential.

However, each of the two gauges (24),(25) is incompatible with the solution method discussed in the present work, since the transparent boundary condition was constructed under the assumption of force-free propagation outside a finite computational volume. We therefore choose to solve the TDSE in the KH frame [23, 24],

$$i\partial_t\psi_{acc}(\mathbf{r},t)=\left[-\frac{1}{2}\Delta+V(|\mathbf{r}-\xi(t)|)\right]\psi_{acc}(\mathbf{r},t), \tag{26}$$

where $\xi(t)$ is the quiver radius of an unbound particle in the laser field. Whenever we drop the gauge index on the wavefunction in the following, we refer to the KH frame. Only the indices $(\cdot)_{len}$ and $(\cdot)_{vel}$ will strictly be used.

The TDSE (26) is compatible with the introduced numerical algorithm if we extend the requirement (2) to

$$V(|\mathbf{r}-\xi(t)|)=0 \qquad \forall t, r\geq R. \tag{27}$$

We now restrict attention to computations with azimuthal symmetry, $V_l^m(r,t)=0\ \forall m\neq 0$. This means

a restriction to linearly polarized laser-fields, such that $\xi$ oscillates along the $z$-direction, along which $\cos(\theta) = -1, 1$. We choose the time dependence of the electric field to be

$$\mathbf{E}(t) = E_0\Theta(t)sin(\omega t)\mathbf{e}_z, \tag{28}$$

where $\Theta$ is the Heaviside function and $\mathbf{e}_z$ is the unit vector in positive $z$-direction. The quiver radius is then given by $\xi(t) = E_0\mathbf{e}_z\Theta(t)sin(\omega t)/\omega^2$. As there is no coupling of partial waves with different quantum numbers $m, m'$ by the field (28), we only solve for the functions $\phi_l^m$ with $m = 0$.

As the initial wavefunction, we choose the ground-state eigenfunction of the unperturbed Potential $V(r)$. In length gauge, the ground state of a central potential will always be spherically symmetric, and can thus be found by integrating the Schrödinger equation

$$i\partial_t {\phi_{len}}_0^0(r,t) = \left[-\frac{1}{2}\partial_r^2 + V(r)\right] {\phi_{len}}_0^0(r,t)$$

with an arbitrary ${\phi_{len}}_0^0(r,0)$ in negative imaginary time over a sufficient number of timesteps and afterwards renormalising the resulting wavefunction. This method of finding the ground state wavefunction is discussed in more detail in [7]. After this procedure, the ground state wavefunction has to be transformed from the length gauge into acceleration gauge. With the laser-field given as (28), the transformation rule is

$$\psi_{acc}(\mathbf{r},0) = \exp\left(-i\frac{E_0 z}{\omega}\right)\psi_{len}(\mathbf{r},0),$$

which translates into the rule

$${\phi_{acc}}_l^0(r,0) = {\phi_{len}}_0^0(r,0)\frac{\sqrt{2l+1}}{2}\int_{-1}^{1} dx P_l(x)e^{-iE_0 rx/\omega}.$$

for calculating all initial partial waves in acceleration gauge. Here, $P_l$ are the Legendre polynomials.

The CN-scheme (23) was solved in the dimensions $l, y$ by a 2D ADI approach [28], and all computationally expensive tasks which give results that can be re-used in more than just one simulation were solved in preprocesses. Those preprocesses covered the numerical determination of the Wigner $3j$-symbols appearing in (17), the integral kernels $\mu_l(R,\tau)$ from (21) for a fixed value of $R$, and the coefficients $V_l^m$. The latter ones were computed by numerical integration of (14) for fixed positions $\xi_y = y\Delta r\mathbf{e}_z,\ y = -(Y+1)\dots Y+1$ of the potential minimum, and for all $l = 0\dots 2L, r = r_y, y = 0\dots Y$. The coefficients $V_l^m(r,t)$ for arbitrary positions of the potential minimum (arbitrary $t$) were then linearly interpolated from this list at runtime of the main program. The preprocesses needed for the computations shown later in this section took roughly an hour of computation time on a modern standard PC.

Two types of central potentials were used. The first one,

$$V_C(r) = -Z\frac{\varrho - r}{\varrho}\Theta(\varrho - r),$$

is a 3D cone potential, which exactly satisfies (27) for sufficiently low $\xi$. The second type of potential is a regularised Yukawa potential,

$$V_Y(r) = -Z\frac{e^{-(r+\epsilon)/\varrho}}{r+\epsilon},$$

which violates (27) only weakly if the screening length $\varrho$ is not too large. Obviously, the Yukawa potential was chosen to simulate a system as close as possible to an unscreened atomic Coulomb potential while still approximately fulfilling the requirements of the numerical algorithm.

In the following, we will discuss the probability

$$P_l(t) = 4\pi\int_0^R dr|\phi_l^0(r,t)|^2$$

to measure the particle with an angular momentum $\sqrt{l(l+1)}$ inside the volume $r \le R$ at time $t$. It should not be mixed up with the Legendre polynomial defined by the same symbol. In all graphs, the time will be normalised by the period $T = 2\pi/\omega$ of the laser field.

The first simulation was carried out using the cone potential with a depth $Z = 0.25$ and a range $\varrho = 5$. For the laser field, we have chosen $E_0 = 0.004, \omega = 0.02$, and the grid parameters were $L = 15, R = 50, \Delta r = 0.1, \Delta t = 0.5$. The resulting histories of occupation probabilities can be seen in Fig. 2. After an initial transient time of about one laser period, the overall probability $\sum_l P_l$ shows a stable exponential decay. However, the very smooth function $\sum_l P_l$ turns out to be the result of a dynamical interplay of partial waves and a continuous transfer of occupation probability between them. At all half-integer multiples of the laser period $T$, the quiver radius $\xi(t)$ vanishes, and the potential is centered around $r = 0$ in (26). Since in the vicinity of $r = 0$, the centrifugal barrier $l(l+1)/(2r^2)$ becomes very large, the partial waves with finite $l$ cannot occupy this space and hence show a dip in their occupation probabilities. The occupation probabilty that was shared among the partial waves with $l \ge 1$ is then transferred to the partial wave $l = 0$, which can be observed as a clear peak in $P_0(t)$ at all $t = nT/2,\ n\epsilon\mathbb{N}$. At the interjacent times $t = T/2(n + 1/2)$, an inverse effect can be observed. At these times, the potential has travelled to its maximum displacement $\xi_{max} = \pm E_0\mathbf{e}_z/\omega^2$. The wavefunction, which follows the attractive potential, is then going to show a pronounced maximum around $\mathbf{r} = \xi_{max}$, with relatively large expansion coefficients for high $l$.

The two mentioned effects can also be seen by directly observing the partial waves $\psi_l^0(r,t) = \phi_l^0(r,t)/r$ for $l =$

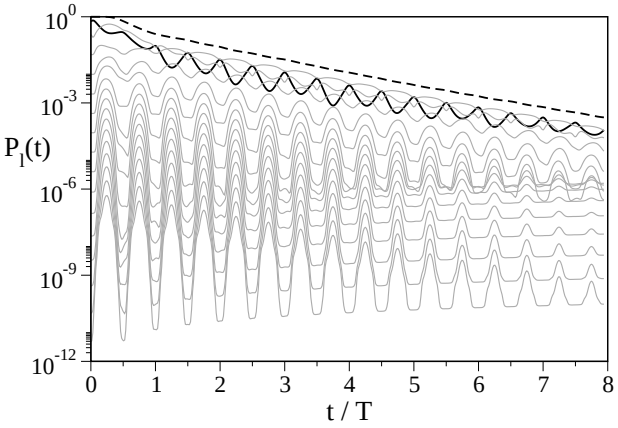


FIG. 2: Time history of occupation probabilities. Dashed: total probability $\sum_l P_l$, solid line: $l = 0$, grey: $l = 1 \ldots 15$. System parameters: $E_0 = 0.004, \omega = 0.02$, cone-potential with $Z = 0.25, \varrho = 5$. Simulation parameters: $L = 15, R = 50, \Delta t = 0.5, \Delta r = 0.1$.

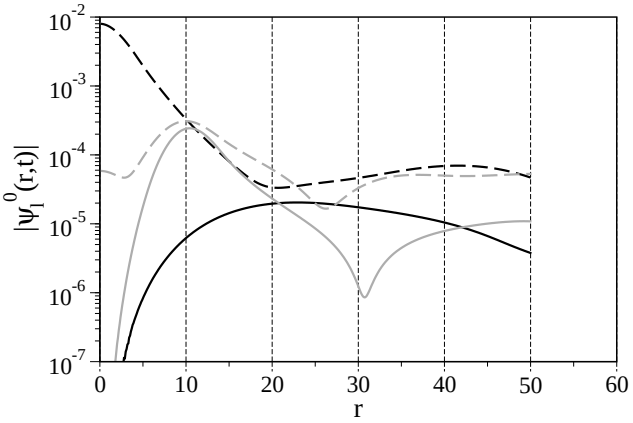


FIG. 3: Snapshots of the partial waves $\psi_l^0(r,t) = \phi_l^0(r,t)/r$ for $l = 0$ (dashed) and $l = 5$ (solid lines). Black curves correspond to $t = 3T$, grey curves to $t = 3.25T$. All simulation parameters are the same as in Fig. 2.

$0, 5$ and $t = 3T, 3.25T$ in Fig. 3. At time $t = 3T$, the partial wave $\psi_5^0$ attains very low values throughout the computational volume, while $\psi_0^0$ peaks around $r = 0$. At time $t = 3.25T$, both functions show peaks around $r = |\xi_{max}| = 10$, and the magnitude of the partial wave $\psi_5^0$ has increased considerably compared to the earlier time $3T$. Note also the smooth form of both partial waves near the boundary $r = 50$, indicating that the boundary condition is preventing any reflections, as expected.

We have used the same system to check for the rate of convergence of the expansion (3) with realistic simulation

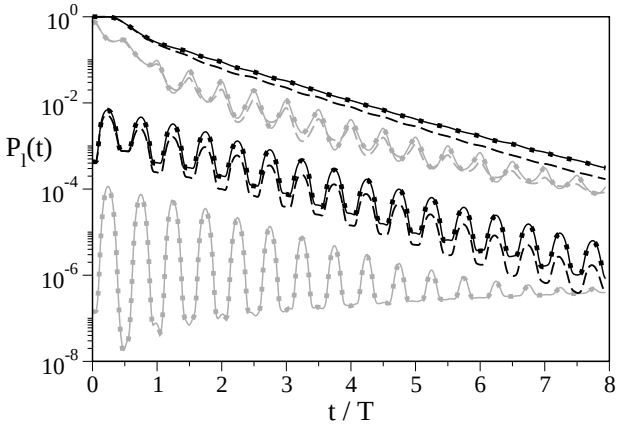


FIG. 4: Time history of occupation probabilities. Solid lines: $L = 15$, dotted: $L = 10$, dashed: $L = 5$. The functions $\sum_l P_l$ (uppermost, black) and $P_0, P_5, P_{10}$ are displayed from top to bottom, in alternating shades of grey. All other parameters are the same as in Fig. 2.

parameters. The result can be seen in Fig. 4, which shows that a truncation of the expansion at $L = 5$ still leads to large deviations from the correct solution, while a truncation at $L = 10$ or $L = 15$ leads to results in very good accordance. This means that convergence is achieved around $L = 10$, for all practical purposes. The reason for this fast convergence has been clearly pointed out by Cormier and Lambropoulos in [12]. They have shown that in the length gauge, the population of partial waves decreases only slowly as a function of $l$, while it decreases rapidly in the velocity gauge, and argue that truncation of a rapidly decaying series will naturally lead to a smaller error than truncation of a slowly converging series. The rapid decrease of population as a function of $l$ is also observed in acceleration gauge (c.f. Fig. 2), so that we can adopt the same argument.

As mentioned in Sec. III, the computational effort to solve one timestep of the numerical algorithm will increase linearly in time, due to the evaluation of the convolution integral (8) in each timestep. The total computation time will therefore be a quadratic function of the number of timesteps $X$. It should be checked how steep this increase in computational effort over time is, as it could spoil long-time computations if the evaluation of the boundary condition becomes numerically too expensive. We have simulated the same physical system with a cone potential as mentioned before, solving for partial waves up to $l = 10$ over 20.000 timesteps, and have recorded the computation time per timestep. The resulting Fig. 5 shows that the computation time per timestep increases only slightly from 0.36 sec to 0.37 sec in the course of the complete simulation. The computational workload generated by the transparent boundary

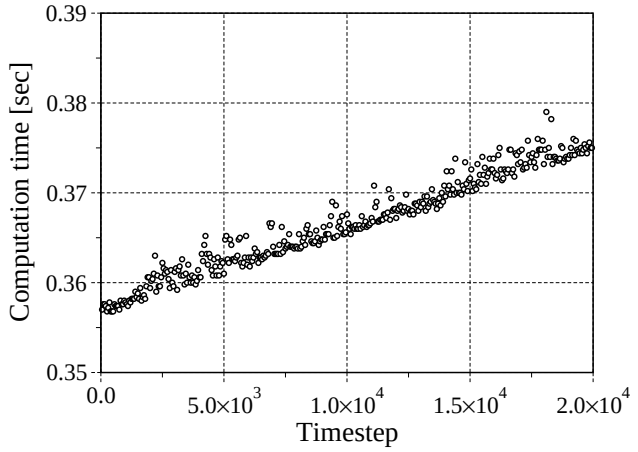


FIG. 5: The time to solve one timestep of the simulation increases linearly in time due to the evaluation of the convolution integral (8) in each timestep. Simulation parameters: $L = 10, R = 50, \Delta_r = 0.1, \Delta t = 0.5$. All System parameters are the same as in Fig. 2.

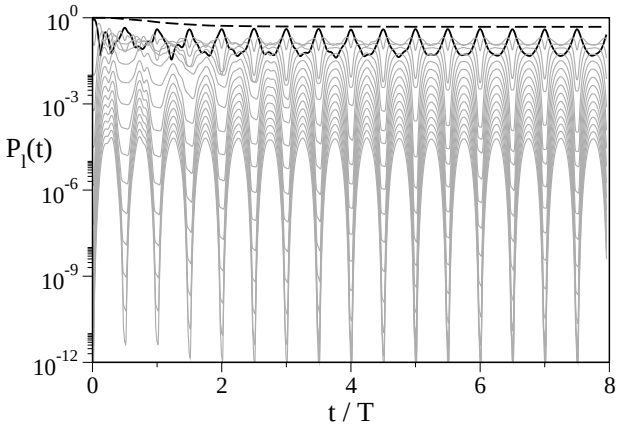


FIG. 6: Time history of occupation probabilities. Dashed: total probability $\sum_l P_l$, black: $l = 0$, grey: $l = 1 \ldots 15$. System parameters: $E_0 = 0.004, \omega = 0.02$, Yukawa potential with $Z = 1, \epsilon = 1, \varrho = 20$. Simulation parameters: $L = 15, R = 50, \Delta t = 0.1, \Delta r = 0.1$.

conditions can therefore safely be assumed to be a minor contribution to the total workload in any of the computations shown in this work, the longest ones of which have taken a few hours of execution time on a modern standard PC.

Since we have shown that our algorithm produces physically meaningful results in the case of the strictly finite-range cone potential, we will now turn to simulations regarding Yukawa potentials, which are a more suitable model for single-atom ionization. In a first computation, we have chosen a regularised Yukawa potential with $Z = 1, \epsilon = 1, \varrho = 20$ in the same laser field that was also used in Fig. 2-4, namely $E_0 = 0.004, \omega = 0.02$. In Fig. 6, we can observe qualitatively the same transfer of occupation probability between partial waves as in the earlier studied system. The overall occupation probability $\sum_l P_l$, however, reduces much slower in time than in Fig. 2. This is simply due to the much more attractive Yukawa potential, which reaches a minimum value of $V_Y(r = 0) \approx -0.95$, as opposed to $V_C(r = 0) = -0.25$ for the potential used in the earlier computation. Convergence of the expansion (3) is again reached for $L \approx 10 \ldots 15$, as can be seen from Fig. 7.

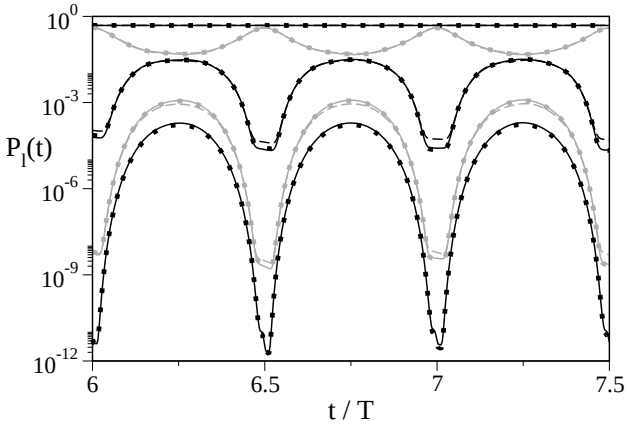


FIG. 7: Time history of occupation probabilities. Solid lines: $L = 15$, dotted: $L = 13$, dashed: $L = 10$. The functions $\sum_l P_l$ (uppermost, black) and $P_0, P_5, P_{10}, P_{13}$ are displayed from top to bottom, in alternating shades of grey. All other parameters are the same as in Fig. 6.

To observe a higher rate of ionization, we have performed one more computation with the same Yukawa potential, this time in a laser field of higher frequency $\omega = 0.05$ and higher amplitude $E_0 = 0.025$. The resulting occupation probabilites are shown in Fig. 8, which shows the desired stronger ionization from a dynamical steady-state that is reached only after a remarkably long equilibration time of 10 to 15 laser periods. The total simulated time was 20 laser periods, which amounts to roughly 2.500 atomic time units or 25.000 time steps.

In such long-time computations the transparency of the boundary is especially important, since reflections from the boundary might cumulate over time in the compuational domain and could thereby completely deteriorate the solution. We have therefore repeated the same

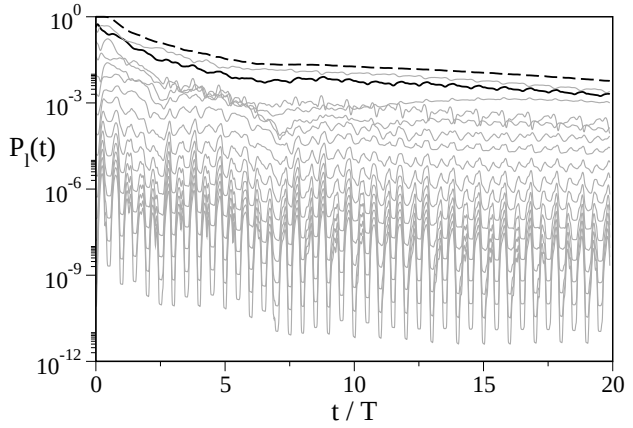


FIG. 8: Time history of occupation probabilities. Dashed: total probability $\sum_l P_l$, black: $l = 0$, grey: $l = 1 \ldots 15$. System parameters: $E_0 = 0.025, \omega = 0.05$, Yukawa potential with $Z = 1, \epsilon = 1, \varrho = 20$. Simulation parameters: $L = 15, R = 50, \Delta t = 0.1, \Delta r = 0.1$.

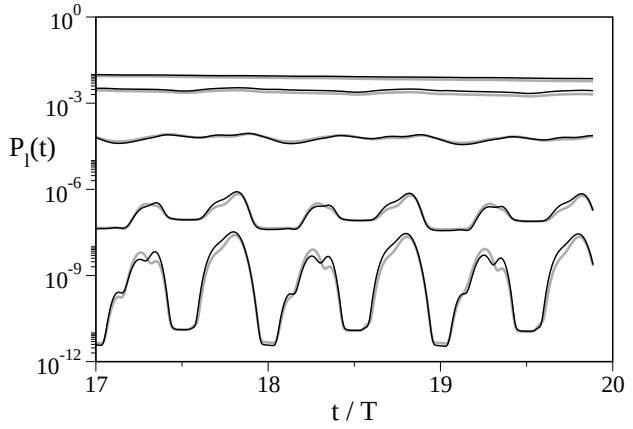


FIG. 9: Time history of occupation probabilities inside the volume $r \leq 50$. Black: $R = 100$, grey: $R = 50$. The functions $\sum_l P_l$ and $P_0, P_5, P_{10}, P_{15}$ are displayed from top to bottom. All other parameters are the same as in Fig. 8.

computation on a grid with an extended radius, $R = 100$. The violation of (27) at this high radius is much weaker than in the first computation with $R = 50$, and the solution can therefore be taken as a reference that should be much closer to the asymptotic solution on an infinite grid, $R \to \infty$. Fig. 9 shows that the deviations between the two solutions remain very small, even towards the end of the computation, and thereby justifies the use of a grid with $R = 50$ in this case.

## V. CONCLUSION

We have presented a numerical method for solving the single particle TDSE inside a sphere with radiation boundary conditions on the sphere. This method is particularly well-suited for dealing with outgoing wave solutions on a finite-size numerical grid. Some constraints of the method arise from (i) the assumption of zero inital and potential values exterior to the sphere, (ii) the use of spherical coordinates along with a partial wave expansion in spherical harmonics, (iii) the calculation in the KH frame. The spherical harmonics expansion in the KH frame is usually convergent for $10 - 15$ angular momentum states for the quiver amplitudes considered. Within this framework, it has been demonstrated, that accurate and efficient numerical solutions of photoionization can be achieved over a relatively long pulse duration of 20 laser cycles at optical frequencies within a small computational volume corresponding to the range of the atomic interaction.


[1] K. C. Kulander, Phys. Rev. A **35**, 445 (1987).
[2] M. S. Pindzola, G. J. Bottrell, and C. Bottcher, J. Opt. Soc. Am. B **7**, 659 (1990).
[3] J. Crank and P. Nicolson, Proc. Camb. Phil. Soc. **43**, 50 (1947).
[4] E. Cormier and P. Lambropoulos, J. Phys. B: At. Mol. Opt. Phys. **30**, 77 (1997).
[5] H. Bachau, E. Cormier, P. Decleva, J. E. Hansen, and F. Martín, Rep. Prog. Phys. **64**, 1815 (2001).
[6] H. Muller, Laser Physics **9**, 138 (1999).
[7] D. Bauer and P. Koval, Comput. Phys. Commun. **174**, 396 (2006).
[8] H. G. Muller and F. C. Kooiman, Phys. Rev. Lett. **81**, 1207 (1998).
[9] E. S. Smyth, J. S. Parker, and K. Taylor, Comput. Phys. Commun. **114**, 1 (1998).
[10] M. D. Feit, J. A. Fleck, Jr., and A. Steiger, J. Comput. Phys. **47**, 412 (1982).
[11] M. E. Riley and B. Ritchie, Phys. Rev. A **59**, 3544 (1999).
[12] E. Cormier and P. Lambropoulos, J. Phys. B: At. Mol. Opt. Phys. **29**, 1667 (1996).
[13] D. Neuhauser and M. Baer, J. Chem. Phys. **90**, 4351

(1989).
[14] M. S. Child, Molecular Phys. **72**, 89 (1991).
[15] C. W. McCurdy and C. K. Stroud, Comp. Phys. Comm. **63**, 323 (1991).
[16] J. L. Krause, K. J. Schafer, and K. C. Kulander, Phys. Rev. A **45**, 4998 (1992).
[17] B. Engquist and A. Majda, Math. Comput. **31**, 629 (1977).
[18] K. Boucke, H. Schmitz, and H.-J. Kull, Phys. Rev. A **56**, 763 (1997).
[19] M. Mangin-Brinet, J. Carbonell, and C. Gignoux, Phys. Rev. A **57**, 3245 (1998).
[20] A. M. Ermolaev, I. V. Puzynin, A. V. Selin, and S. I. Vinitsky, Phys. Rev. A **60**, 4831 (1999).
[21] X. Antoine and C. Besse, J. Comput. Phys. **188**, 157 (2003).
[22] M. Heinen and H.-J. Kull, Phys. Rev. E **79**, 056709 (2009).
[23] H. A. Kramers, *Collected Scientific Papers* (North-Holland, Amsterdam, 1956).
[24] W. C. Henneberger, Phys. Rev. Lett. **21**, 838 (1968).
[25] L. Dimou and H.-J. Kull, Phys. Rev. A **61**, 043404 (2000).
[26] M. Abramowitz and I. A. Stegun, *Handbook of Mathematical Functions* (Dover Pub., New York, 1965).
[27] A. Messiah, *Quantum mechanics 2* (North Holland, Amsterdam, 1962).
[28] L. Lapidus and G. F. Pinder, *Numerical solution of partial differential equations in science and engineering* (J. Wiley, New York, 1982).
[29] R. Shakeshaft Z. Phys. D **8**, 47 (1988).